Journal of the European Ceramic Society 41 (2021) 290–298

Contents lists available at ScienceDirect

Journal of the European Ceramic Society

journal homepage: www.elsevier.com/locate/jeurceramsoc

Unravelling the optimization of few-layer graphene crystallinity and electrical conductivity in ceramic composites by Raman spectroscopy

Carmen Muñoz-Ferreiro [a,b,c], Cristina López-Pernía [a], Ángela Gallardo-López [a], Rosalía Poyato [c,*]

[a] Dept. de Física de la Materia Condensada, ICMS, CSIC-Universidad de Sevilla, Apdo. 1065, 41080, Sevilla, Spain
[b] Université de Lyon, INSA Lyon, MATEIS UMR CNRS 5510, 7 Avenue Jean Capelle, F-69621, Villeurbanne Cedex, France
[c] Inst. Ciencia de Materiales de Sevilla, ICMS, CSIC-Universidad de Sevilla, Américo Vespucio 49, 41092, Sevilla, Spain

ARTICLE INFO

Keywords:
Few-layer graphene
Composites
Crystallinity
Raman spectroscopy
Electrical conductivity

ABSTRACT

Zirconia composites with few-layer graphene (FLG) were prepared by two powder processing routines -ultrasonic agitation or planetary ball milling- and spark plasma sintered at 1250 and 1300 °C. An in-depth study of the crystallinity of FLG, in terms of presence and nature of defects, was performed by Raman spectroscopy, revealing enhanced FLG crystallinity after sintering. This enhancement was more noticeable in the composites sintered at the highest temperature, with lower amount of structural defects and amorphous carbon. However, remaining amorphous carbon was detected in the composites prepared by planetary ball milling even after sintering at the highest temperature, resulting in lower electrical conductivities. Optimum results in terms of electrical conductivity were achieved for the composites prepared by ultrasonic agitation and sintered at 1300 °C, with electrical percolation limit below 2.5 vol% FLG and high electrical conductivity (678 S/m for 5 vol% FLG), as result of the enhanced FLG crystallinity after sintering.

1. Introduction

During the last decade, the research on graphene reinforced ceramics has attracted increasing attention on the scientific and engineering communities. As consequence of the exceptional mechanical, thermal or electrical properties of the graphene-based nanomaterials (GBN), enhanced properties are promoted in these ceramic composites [1–3]. On the one hand, a toughening of the matrix is pursued, so the inherent fragility of ceramics can be overcome, resulting in suitable materials for advanced structural applications [4–6]. On the other hand, tailoring of the functional properties –as electrical and thermal conductivity– is searched [7–9]. Achieving high electrical conductivities by the incorporation of GBN allows the manufacturing of miniaturized complex shapes by the electrical discharge machining of ceramics that are electrically insulating, and usually hard to machine using the conventional manufacturing tools [10,11]. This would allow the implementation of these materials in applications such as micro-electro-mechanical systems (MEMS).

The GBN usually incorporated as second phase in ceramic composites include multilayer graphene (MLG, up to 10 graphene layers), few-layer graphene (FLG, 2–5 layers) and also cost-effective thicker stacks of more than 10 graphene layers, with a maximum thickness around 100 nm, known as graphene nanoplatelets (GNP). Although the use of advanced powder processing techniques that promote the exfoliation and homogenization of the thicker GNP –such as planetary ball milling or microfluidization– have resulted in enhanced properties in ceramic composites with GNP [7,12,13], in general, the best results in terms of mechanical and electrical properties have been obtained in composites with FLG [9,14] or reduced graphene oxide (rGO) [8,15,16].

When using FLG as second phase, the good results have been related by several authors to the higher interface area and better homogeneous dispersion in the ceramic matrix in comparison with the thicker GNP [9,14]. Moreover, Ahmad et al. [4] related the enhancement in fracture toughness in Al_2O_3 composites to the formation at the interface Al_2O_3-graphene nanosheet of an intermediate aluminum oxycarbide phase that facilitates efficient load transfer. The higher values of electrical conductivity obtained in composites with FLG, in comparison with composites with GNP, have been also related to the strong dependence of the conductivity of graphene-based nanomaterials with the number of graphene layers [9,17], with higher conductivities in GBN with lower

* Corresponding author.
E-mail address: rosalia.poyato@icmse.csic.es (R. Poyato).

https://doi.org/10.1016/j.jeurceramsoc.2021.09.025
Received 30 June 2021; Received in revised form 8 September 2021; Accepted 10 September 2021
Available online 16 September 2021

number of layers [18], as FLG.

In composites with rGO as second phase, different authors have related the enhanced properties in SiC composites to a better delamination of the graphene layers during the preparation process as a consequence of the higher interplanar distance between the graphene layers in GO [8], or to the intimate contact of the rGO with the ceramic grains, by forming C–O–Al or COOAl bonding without any interfacial phases in Al_2O_3 composites [19]. In some works, the reduction of the GO has been *in-situ* produced during sintering of the composites by Spark Plasma Sintering (SPS) or Rapid Hot Pressing (RHP) [5,6,8,16,20]. Zeng et al. [5] reported a higher fracture toughness for the *in-situ* reduced GO/zirconia composites, in comparison with the composites with pre-reduced graphene oxide, which was attributed to the formation of a C-O-Zr bond at the interface. Ramirez et al. [6] pointed to a possible strong chemical bonding as responsible for the extraordinary toughness of *in-situ* reduced GO/Si_3N_4 nanocomposites.

Some authors have suggested that the properties enhancement in ceramic composites could be even better by the optimization of the crystallinity of graphene through better-controlled GO reduction protocols or accurately tailored sintering conditions in composites with FLG [6,21,22]. However, the number of works devoted to these kind of studies is scarce. Inam et al. [21] showed that graphene in Al_2O_3 nanocomposites SPSed and HPed using longer durations (60 min) possessed higher crystallinity, resulting in composites with enhanced thermal stability and electrical conductivity, in comparison with SPSed samples sintered using shorter sintering durations (10–20 min). This was attributed to the thermally induced graphitization caused by longer sintering protocols. Wang et al. [22] reported that graphene structure stability in HPed Al_2O_3-based composites was highly dependent on the sintering temperature and dwell time, as high sintering temperature and extended dwell time could destruct the graphene structure stability. In addition, a too shortened dwell time was also detrimental to the graphene structure stability due to the insufficient crystallinity.

Raman spectroscopy is a powerful technique for the analysis of the crystallinity and the defect structure of graphitic materials, and it has been widely used to characterize graphite, pristine and defective graphene or graphene oxide. Whereas the Raman spectrum in pristine graphene presents two main bands at ~1585 cm^{-1} (G band) and ~2700 cm^{-1} (2D band) -associated with first- and second-order allowed Raman modes, respectively-, new Raman bands appear in the spectrum when the periodicity of the graphene lattice is broken by defects [23–28]. Thus, the presence of these bands and their positions and intensities provide information about the existence and nature of defects in graphene-based nanomaterials [25,26,29]. Among the defect-induced bands, the most prominent one is situated at ~1350 cm^{-1} (D band), and the intensity ratio I_D/I_G is extensively used to characterize the level of defects in graphene. Together with the appearance of defect-related bands, the presence of defects can also modify the intensity ratio, bandwidths and/or positions of the G and 2D bands [25]. In the field of ceramic composites with graphene, Raman spectroscopy is extensively used to discard the generation of defects in graphene during the sintering process [9,30,31] or to characterize the *in-situ* reduction of graphene oxide [5,15,16,20]. However, in order to elucidate the optimization of the graphene crystallinity promoted by the composite sintering thermal treatments and to relate it to the enhancement of the composite properties, it is essential to properly establish the defect structure of graphene by means of a thorough analysis of the different Raman bands, their positions, intensities and shapes and their evolution after the sintering process.

In this work, the influence of the processing conditions –powder processing routine and sintering temperature– of zirconia composites with few-layer graphene on the crystallinity of FLG and its relationship with the electrical conductivity of the composites has been analyzed. To that end, composite powders have been prepared using two different routines -ultrasonic agitation or planetary ball milling- and have been Spark Plasma Sintered at two different temperatures. The crystallinity of FLG, in terms of presence and nature of defects, before and after the sintering process has been thoroughly analyzed by Raman spectroscopy. The electrical conductivity of the composites has been determined and related to the microstructural features.

2. Experimental procedure

2.1. Composite powders processing and characterization

Few-layer graphene (FLG) with n ≤ 3 graphene layers and ≤ 10 μm planar diameter (Angstron Materials, Dayton, Ohio, USA) and 3 mol% yttria tetragonal zirconia polycrystal (3YTZP) ceramic powder with 40 nm particle size (Tosoh Corporation, Tokyo, Japan), previously annealed at 850 °C for 30 min in air, were used as the starting materials for the preparation of the composites. Two different powder processing routines were used to prepare composite powders with 2.5 and 5 vol% FLG:

Ultrasonic agitation (UA): a suspension of the FLG in isopropyl alcohol was subjected to ultrasonic agitation for 15 min by means of an ultrasonic bath. The 3YTZP powder was added to the FLG suspension and sonicated for 5 min in order to homogenize the mixture. After drying on a hot plate with continuous magnetic stirring, the composite powders were homogenized in an agate mortar.

Planetary ball milling (PBM): a suspension of the FLG and the 3YTZP powder in a 10 wt% tert-butanol (t-BuOH)/water mixture was homogenized in a planetary ball mill (Pulverisette 7, Fritsch, Germany), at a speed of 150 rpm for 15 min. The milling media consisted of seven 15 mm diameter zirconia balls in a 45 mL zirconia vial. The slurry was dried on a hot plate with continuous magnetic stirring and the powders were homogenized in an agate mortar.

Raman spectroscopy was used to characterize the as-received FLG and the composite powders in order to account for possible structural modifications after the composite powder processing. At least ten spectra were acquired on each sample using a dispersive microscope Raman Horiba Jobin Yvon LabRam HR800, with a green laser He-Ne (532.1 nm) at 20 mW (Instituto de Ciencia de Materiales de Sevilla, ICMS). The microscope used a 100x objective and a confocal pinhole of 100 μm. The first-order (from 1000 to 2000 cm^{-1}) Raman spectra were fitted to a sum of five functions -two Gaussian and three pseudo-Voigt functions-. In the second-order spectra (from 2250 to 3500 cm^{-1}) four pseudo-Voigt functions were used. The fits were carried out using the Origin software.

2.2. Composite sintering and characterization

The composite powders were spark plasma sintered at 1250 and 1300 °C for 5 min, with an applied pressure of 75 MPa (SPS model 515 S, Dr. Sinter, Inc., Kanagawa, Japan, Functional Characterization Service, Centro de Investigación, Tecnología e Innovación de la Universidad de Sevilla, CITIUS). The temperature was monitored by means of an optical pyrometer focused on the side of the graphite die. A sheet of graphite paper was placed between the powders and the die/punches to ensure their electrical, mechanical and thermal contact and also for easy removal. The obtained composites (~15 mm diameter, ~3 mm thickness) were manually grinded to remove the graphite paper from the SPS moulding system.

The density of the composites was measured with the Archimedes' method using distilled water as the immersion medium. The theoretical density for the different composites was calculated by the rule of mixtures taking the density of the 3YTZP and the FLG as 6.05 g/cm^3 and 2.2 g/cm^3, respectively (data from the suppliers). The possible structural modifications of the FLG in the composites after the sintering process were assessed by Raman spectroscopy. To that end, at least ten spectra were acquired on the polished cross section surfaces of the different composites. The first-order Raman spectra were fitted to the five functions previously described in §2.1. In the second-order spectra,

the best fit was achieved by using three Lorentz functions and three pseudo-Voigt functions.

To characterize the distribution of the FLG in the ceramic matrix, cross-section (c.s.) surfaces of the composites were polished with diamond paste up to 1 μm and analyzed by low magnification conventional scanning electron microscopy (SEM, FEI-Teneo, FEI, USA, CITIUS) using backscattered electrons (BSE) for imaging.

The grain size of the ceramic matrix was estimated from SEM images acquired on polished c.s. surfaces previously annealed for 15 min in air at a temperature 100 °C lower than the composite sintering temperature. The equivalent planar diameter, $d = 2(\text{area}/\pi)^{1/2}$, namely the diameter corresponding to a circle with the same area as the measured grain, was taken as a measure of the ceramic grain size. The shape factor of the grains was calculated as $F = 4\pi\ \text{area}/(\text{perimeter})^2$. The ImageJ and Origin softwares were used to quantify these morphological parameters, averaging 200–300 grains, according to UNE-EN ISO 13383-1:2016 standard.

The electrical conductivity of the composites was estimated using the capacitive method. To that end, the samples were cut into parallelepipedic specimens, two parallel faces were coated with colloidal silver paste, and the electrodes were fired at 600 °C for 30 min under Ar flow to avoid any degradation of the FLG during the process. The measurements were performed at room temperature in a two-point configuration. In order to account for any degree of electrical anisotropy in the composites, two different electrode configurations were used to obtain the electrical conductivity in the directions parallel ($\sigma_{//}$) and perpendicular ($\sigma_{\perp}$) to the compression axis during SPS. Two different equipments were used to validate the obtained results of the electrical conductivity: An Agilent 4294A analyzer in the 100 Hz - 2 MHz frequency range and a Solartron SI1260A, which used a potentio-dynamic method with a 0−10 mV range in steps of 1 mV (Functional Characterization Service, CITIUS). The measurements were validated also in AC, with a frequency sweep from 100 to 1000 Hz at 10 mV. With the potentio-dynamic method, several measurements were taken in each configuration. For each measurement, the electrodes were removed with acetone and new colloidal silver paste was applied and fired.

3. Results and discussion

3.1. Raman spectroscopy study

3.1.1. As-received FLG and composite powders

The analysis of the Raman spectrum from the as-received FLG is essential in order to subsequently establish the possible modifications in crystallinity after the composite powder processing and sintering.

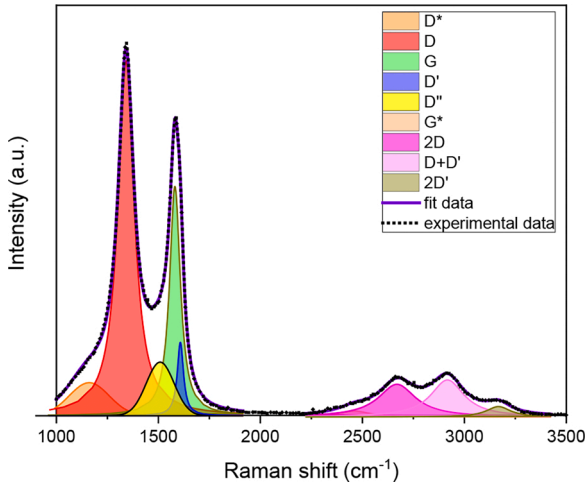

Fig. 1. Raman spectrum acquired on the as-received FLG powder. An example of the deconvolution of the first- and second-order Raman spectra is included.

Fig. 1 presents a representative Raman spectrum from the as-received FLG powder. This spectrum presents some differences with respect to the published one for pristine graphene. Sharp and well-defined G and 2D bands are observed at ~ 1590 and ~ 2700 cm^{-1}, respectively, for pristine graphene [24,27,32]. However, for the as-received FLG two broadened D and G bands can be observed in the range 1000−2000 cm^{-1}, and several low-intensity overlapped peaks are found in the range 2250−3500 cm^{-1}. Thus, several features present in the spectrum in Fig. 1 reveal that the as-received FLG is very likely defective graphene [25,29]. The D band (~ 1350 cm^{-1}) –the most prominent defect-related band– presents a high intensity and a shoulder on the low-frequency region. Moreover, a wide feature is observed between the broadened D and G bands. All this is consequence of the presence of other low-intensity bands that are overlapping with the main bands of graphene in this region. Minor bands located at ~ 1100–1200 (named D'' or D*) and ~ 1610 - 1620 cm^{-1} (D') have been reported in literature as also associated to phonon-defect processes in graphene [25–27,29,33,34]. A broad Raman band at ~ 1500 cm^{-1} (named T_2, D_3 or D'' by different authors) has been detected in graphene oxide [20,34,35], carbon nanotubes [36] or other defective carbon-based materials [37–39] and related to the presence of amorphous carbon. Furthermore, the D + D' band (~ 2930 cm^{-1}) –also related to defects– shows a quite high intensity and appears in the spectrum overlapped with the 2D band, which presents a low intensity.

Several authors have pointed out the intensities, widths and positions of the Raman bands as highly dependent on the presence of defects on the GBN structure [25,28,34]. Thus, they are suitable parameters to characterize the level of defects in these nanomaterials. In order to properly obtain these data, it is essential to perform a deconvolution of the Raman peaks [13,28,34,36,38]. In the present work, we will assume the nomenclature D* and D'' for the bands at ~ 1100–1200 and ~ 1500 cm^{-1}, respectively. We have fitted the first-order region to two Gaussian (D* and D") and three pseudo-Voigt (D, G and D') functions, and the second-order region to four pseudo-Voigt functions (G*, 2D, D + D' and 2D'), as suggested by previous authors [13,28,34]. An illustrative example of the fittings is included in Fig. 1. Table S1 in the Supplementary Section presents the relative intensities (by means of integrated areas) of the main defect-related peaks (D, D" and D') and of the 2D band with respect to the G peak. The full-width at half-maximum (FWHM) and the positions for the D, D'', G, D' and 2D peaks obtained from the fittings are also presented in Tables S2 and S3 in the Supplementary Section.

The high values of I_D/I_G and $I_{D'}/I_G$, together with the high values of the FWHM for the D, G, D' and 2D bands, point to the existence of defects and disorder in the as-received FLG. According to the terminology introduced by Ferrari et al. [27,38] to classify disordered graphene with different levels of defects, the as-received FLG ($I_D/I_G = 2.33 \pm 0.04$) would fit into the Stage I in the classification (low-defect graphene), as the transition to the Stage II (disordered graphene) is established at $I_D/I_G = 3.5$. Furthermore, the obtained values of FWHM for the D, G, D' and 2D peaks are similar to the reported ones by Martins-Ferreira et al. [25] for defective graphene with a distance between defects lower than 4 nm, and by Díez-Betriu et al. [28] for partially reduced GO. The low I_{2D}/I_G value is also consequence of the presence of disorder in the as-received FLG, as it has been published that the intensity of the 2D band decreases when the number of defects on the structure increases [25]. The existence of a noticeable D'' band reveals the presence of amorphous carbon, as suggested by previous authors [34,35,37,39].

The spectra acquired on the composite powders prepared by the ultrasonic agitation and the planetary ball milling routines (Fig. S1 in the Supplementary Information) are very similar to the obtained ones for the as-received FLG. No significant changes were observed on the intensity ratios, FWHM or peaks positions (Tables S1, S2 and S3 in the Supplementary Section).

3.1.2. Sintered composites

After sintering, the Raman spectra acquired on the composites present sharper D and G peaks, and a better defined 2D band. Fig. 2 shows representative examples of the acquired Raman spectra and the fittings that were carried out for the composites with 5 vol% FLG sintered at 1300 °C from the powders processed by the UA and the PBM routines. The spectra and fittings from the rest of composites are shown in Fig. S2 in the Supplementary Information. The intensities ratios, FWHM and positions of the peaks obtained from the fittings are presented in Tables S4, S5 and S6 in the Supplementary Section. The best fit for the 2D band was achieved by using three Lorentzian functions. According to Malard et al. [24] and Ferrari et al. [32] this confirms that the graphene-based nanomaterial in the composites presents a number of layers lower than 10.

A remarkable decrease of I_D/I_G and $I_{D'}/I_G$, and a significant increase of I_{2D}/I_G are observed in all the composites when comparing with the data for the as-received FLG (Fig. 3). This reveals a reduction on the number of defects present in the FLG during the thermal treatment [21,25,28,39]. The drastic I_{2D}/I_G increase observed in the 2D peak of reduced graphene oxide after thermal treatment has been attributed by Díez-Betriu et al. [28] to the restoration of the graphene interatomic distances and angles. A decrease of the FWHM for the D, G and D' bands is also observed in all the composites when comparing with the as-received FLG (Fig. 4, numerical data can be found in Table S5). Martins Ferreira et al. [25] have reported lower FWHM for D, G, D' and 2D bands in graphene with a lower number of defects. They also reported that from these four bands, the G and D' peak widths have a less pronounced dependence on the number of defects than the D and 2D bands. In the present study, we have also noticed the less pronounced change on the G and D' bands widths after the sintering treatment (numerical data can be found in Table S5). Moreover, although a clear decrease of the 2D band width is visually observed in Figs. 2 and S2, as this band is the result of several Raman processes for the FLG in the sintered composites, and it has been fitted to three Lorentz functions, it is impossible to obtain data for the 2D band FWHM. Thus, the FWHM of the D peak was chosen in this study as suitable parameter to describe the enhancement on crystallinity, as previously suggested by Díez-Betriu et al. [28]. The FWHM for this band in the sintered composites is ~ 50−60 cm^{-1} (Table S5), the same values as the reported ones for 3YTZP composites with *in-situ* reduced GO [20] and quite close to the published value for highly reduced few-layer graphene oxide films (40 cm^{-1}) [28]. This supports the enhancement in crystallinity of FLG achieved during sintering in all the composites.

Regarding the D'' band at 1500 cm^{-1}, a decrease of both $I_{D''}/I_G$ (Fig. 3(b)) and FWHM (Fig. 4(b)) are observed in all the composites when comparing with the data for the as-received FLG. Different authors have related this band intensity and width to the crystallinity of a carbonaceous material. An increase of $I_{D''}/I_G$ with the proportion of amorphous carbon in soot has been reported by Sadezky et al. [37] and Jawhari et al. [40]. Vollebregt et al. [36] reported a decrease of the D'' peak intensity and width when increasing crystallinity of Multi Wall Carbon Nanotubes (MWNT) grown by chemical vapour deposition at

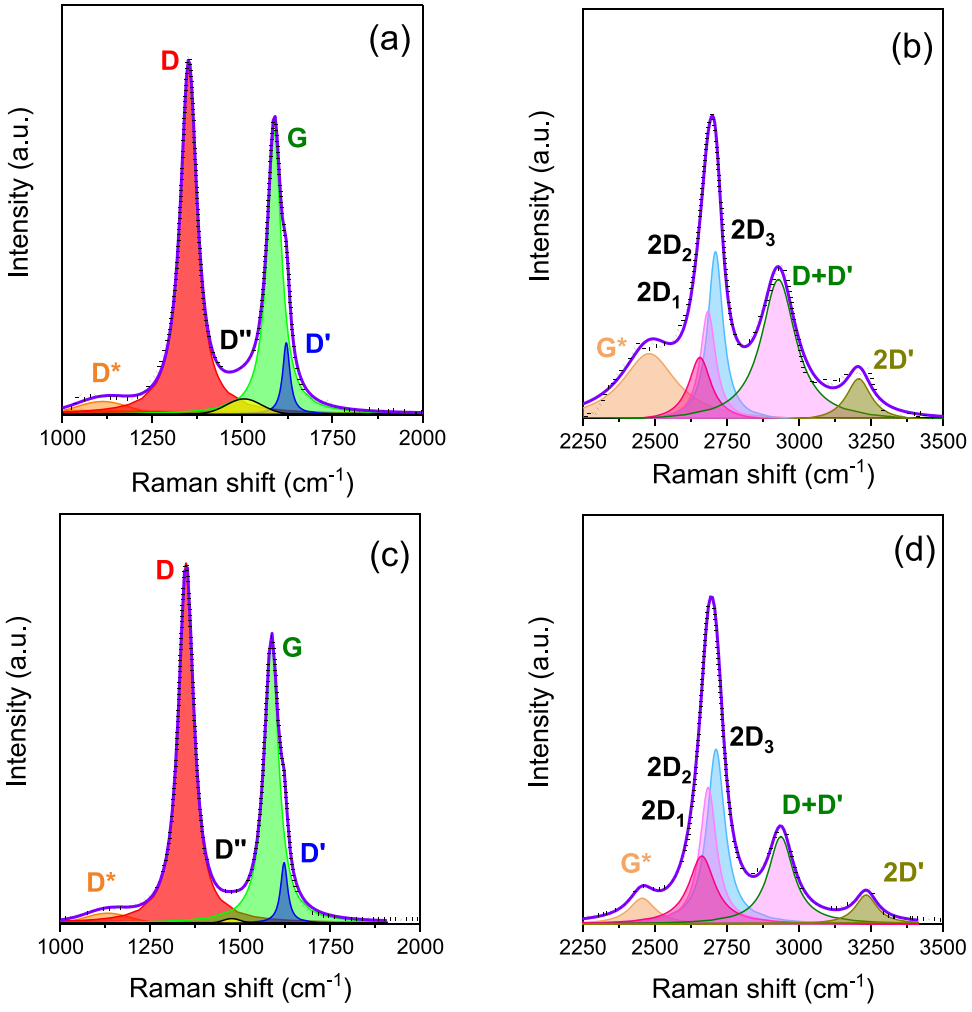

Fig. 2. Deconvolution of the first-order Raman spectra (a) and (c), and the second-order Raman spectra (b) and (d) of the composites with 5 vol% FLG sintered at 1300 °C from powders prepared by (a) and (b) PBM and (c) and (d) UA.

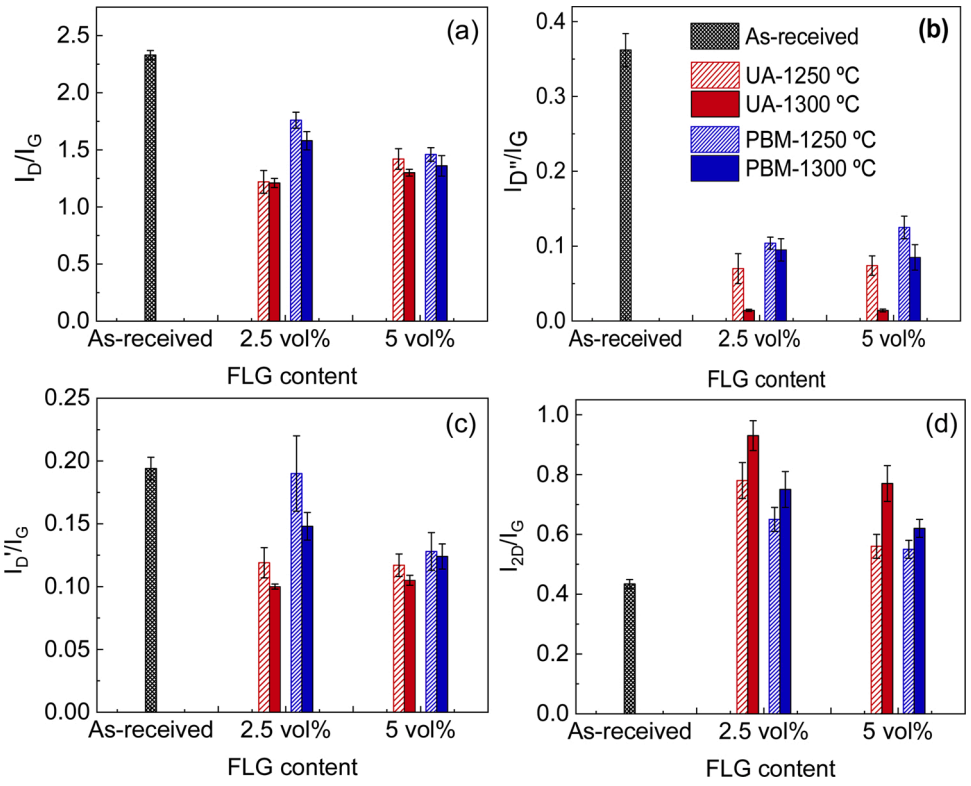

Fig. 3. Intensity ratios of the D, D'', D' and 2D bands with respect to the G peak, obtained for the as-received FLG and the sintered composites; (a) I_D/I_G; (b) $I_{D''}/I_G$; (c) $I_{D'}/I_G$; (d) I_{2D}/I_G.

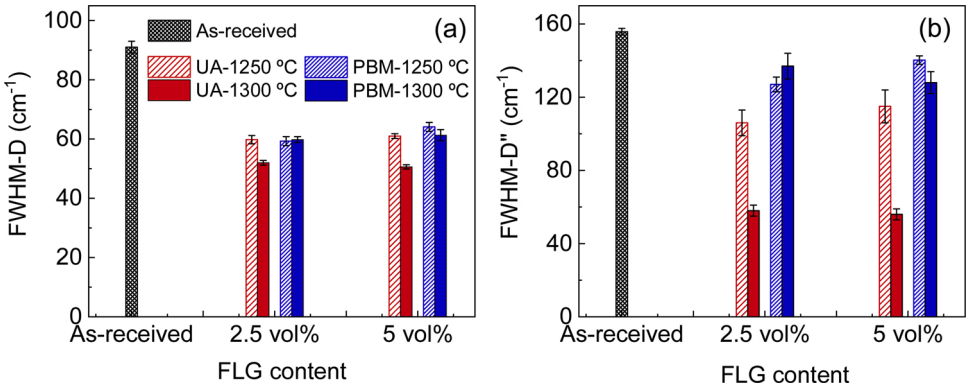

Fig. 4. FWHM of the (a) D and (b) D'' peaks obtained for the as-received FLG and the sintered composites.

growth temperatures between 500 and 750 °C. Claramunt et al. [35] performed a detailed study of this band for reduced graphene oxide, and found a decrease of $I_{D''}/I_G$ and FWHM for reducing temperatures above 200 °C. In our recent studies, we have performed thorough Raman analysis of ceramic composites with *in-situ* reduced GO [20] or with graphene-like nanosheets [39], finding in both cases a significant decrease of $I_{D''}/I_G$ and FWHM(D'') after spark plasma sintering at 1250 °C. Thus, the decrease found in the present study can be related to a decrease in the amount of amorphous carbon present in the FLG after the thermal treatment.

When increasing the sintering temperature from 1250 to 1300 °C, a decrease of the intensity ratios related to defects (I_D/I_G and $I_{D'}/I_G$) and to amorphous carbon ($I_{D''}/I_G$), together with an increase of I_{2D}/I_G are observed in the composites prepared by the two processing routines (Fig. 3). Moreover, a decrease of FWHM for the D and D'' peaks is also observed when sintering at higher temperature (Fig. 4). All this analysis points to an enhanced crystallinity in the composites sintered at the highest temperature, with lower amount of structural defects and amorphous carbon. Previous authors have analyzed the graphene crystallinity in ceramic composites by Raman spectroscopy, reporting that graphene can go through thermally-induced structural transformations which include higher degree of crystallinity or decrease of the content of amorphous carbon during the sintering process [21,22]. However, to the best of our knowledge, this is the first time that the intensity and FWHM of the D'' band have been quantitatively analyzed and related to the graphene crystallinity optimization. Furthermore, this quantitative analysis helps to elucidate the decrease in amorphous carbon present in the FLG achieved by accurately tailoring the sintering temperature.

Significant differences are observed when comparing the composites sintered from the powders prepared by the two different processing routines. Slightly higher I_D/I_G and $I_{D'}/I_G$ ratios, and lower I_{2D}/I_G value are obtained for the composites prepared by PBM, which points to a higher amount of structural defects. However, the most remarkable difference is related to the D'' band. Whereas for the composites

prepared by ultrasonic agitation a huge decrease is observed for $I_{D''}/I_G$ and FWHM (D'') when increasing the sintering temperature, this lowering is not so remarkable for the composites prepared by planetary ball milling (Figs. 3(b) and 4 (b)). The difference of the D'' intensity (estimated from the integrated area) can be visually checked in Fig. 2, as an example, for the composites with 5 vol% FLG sintered at 1300 °C from the powders prepared by the PBM and the UA routines (Fig. 2(a) and (c), respectively). Whereas for the PBM composite this band is perfectly recognized (yellow peak at ~ 1500 cm^{-1}), for the composite prepared by the UA routine this band is almost inexistent. This means that, regardless of the sintering temperature, a certain amount of amorphous carbon is present in the FLG in the composites when using high-energy planetary ball milling during powder processing. On the contrary, when using ultrasonic agitation to prepare the powders, the amorphous carbon is almost completely removed just by increasing the sintering temperature to 1300 °C.

As previously mentioned in section §3.1.1, no significant changes were observed on the intensity ratios, FWHM or peaks positions for the powders prepared by the ultrasonic agitation and the planetary ball milling routines. This could point to a similar amount of defects and amorphous carbon in both powders. However, since the same SPS temperatures were used for the sintering of both types of samples, the difference in the amount of amorphous carbon between the two types of samples cannot be related to the sintering step, but to the powder processing routine. Several authors [41,42] have reported the introduction of defects in the graphene structure during high-energy planetary ball milling. Thus, it can be inferred that defects and amorphous carbon are very likely introduced in the graphene structure during the ball milling of the powder, and cannot be completely removed in the sintered composites just by increasing the sintering temperature. The fact that the higher amount of defects and amorphous carbon in the PBM powders is not detected by the Raman study performed in this work could be related to a lack of resolution of the quantitative Raman study in highly defective FLG as the one analyzed in this study.

In all the composites, the positions of the D, G and D' bands (Table S3) show a ~ 10 cm^{-1} shift to higher frequency, in comparison with the as-received FLG. This is consequence of the residual stresses imposed by the ceramic matrix, as suggested by previous studies [5,21]. A more significant shift is found for the 2D band (~ 20 cm^{-1}), in agreement with Androulidakis et al. [43], who reported higher frequency shifts for the 2D band than for the G band of few-layer graphene under deformation. On the contrary, the position of the D'' band presents a behaviour that is different for the composites prepared by the two routines. While the position of the D'' is shifted towards lower frequencies in the composites prepared by UA, in comparison with the as-received FLG, this position stays invariable in the composites prepared by PBM (Table S3). A shift of the D'' peak position to lower frequencies has been previously detected in ceramic composites with rGO, and has been related to a decrease of the oxygen content and to the subsequent reduction of the GO during the sintering process [20]. Thus, this result also supports that an optimized crystallinity -in terms of structural defects, amorphous carbon and oxygen content- is achieved in the composites prepared by UA, in comparison with the ones prepared by PBM.

In closing, although good results in terms of homogeneous GNP distribution in the ceramic matrix and electrical conductivity have been reported for ceramic composites with graphene nanoplatelets when using high-energy ball milling during powder processing [12], the analysis carried out in this study has revealed that this high-energy milling introduces a certain amount of amorphous carbon, structural defects and oxygen content in the FLG structure that is not possible to remove during the sintering process.

3.2. X-ray diffraction and scanning electron microscopy analysis

Nearly fully dense composites, with relative densities ≥ 97 % and grain sizes ~ 0.25 – 0.5 μm were obtained after SPS (Table 1). All the composites present a similar shape factor (F = 0.7 ± 0.1), which reveals that the ceramic grains are equiaxed. The semi-quantitative XRD analysis performed on the composites revealed that the main phase in all of them was the reduced tetragonal zirconia ($ZrO_{1.95}$), with JCPDS file 081–1544 (not shown). The presence of a reduced tetragonal phase is consequence of the sintering under reducing conditions as reported in previous works [9,20,30].

The FLG distribution in the ceramic matrix has been assessed by low-magnification SEM using backscattered electrons for imaging. In this mode, the 3YTZP matrix and the FLG appear in the micrographs as light and dark phases, respectively, due to the average atomic number difference between the two phases of the composite. Figs. 5 and 6 show the BSE-SEM micrographs of the polished c.s. surfaces of the composites processed by the UA and the PBM routines, and sintered at 1250 and 1300 °C. In all the composites the FLG appears as thin dark lines with a clear alignment. This indicates that the major surface -*ab* plane- of the graphene layers is laying on a plane perpendicular to the compression axis during SPS, and thus, the cross sections show a side view of the FLG. This preferential orientation is consequence of the two-dimensional nature of FLG and the uniaxial pressure applied during sintering, as previously pointed out in literature [9,30]. No significant microstructural differences are found between the composites prepared by the two powder processing routines, as the FLG appears homogeneously distributed throughout the ceramic matrix in all the composites. Therefore, no remarkable effect of the use of the high-energy planetary ball milling is observed in the composites microstructure.

3.3. Electrical properties of the composites

The electrical conductivities in the directions perpendicular ($\sigma_\perp$) and parallel ($\sigma_{//}$) to the pressing axis during SPS for all the composites are presented in Table 2. In all the conductive composites, $\sigma_\perp$ is higher than $\sigma_{//}$, revealing an anisotropic electrical behaviour in all of them independently of the FLG content, the powder processing routine or the sintering temperature. This anisotropy has been reported previously for spark plasma sintered composites with GBN [9,20,30].

For a FLG content of 2.5 vol%, only the composite sintered at 1300 °C from powders prepared by ultrasonic agitation presents electrical conductivity. Therefore, for these processing conditions, the percolation limit is lower than 2.5 vol%. This is clearly related to the optimized crystallinity, in terms of lower amount of structural defects and amorphous carbon, that has been revealed for this composite by the Raman spectroscopy analysis in section §3.1.2. Díez-Betriu et al. [28] have reported that highly reduced few-layer graphene oxide films can reach conductivities of up to 500 S/cm. Thus, just by increasing the sintering temperature and selecting an adequate powder processing routine it is possible to decrease the percolation threshold.

For the UA composites sintered at 1250 °C and the PBM composites sintered at both temperatures, the percolation limit is situated between 2.5 and 5 vol% FLG.

Regardless of the powder processing routine, the highest conductivities were obtained for the composites sintered at 1300 °C, as

Table 1
Relative density of the composites, and mean grain size with its standard deviation of their ceramic matrices.

FLG vol%	Processing routine	Sintering T (°C)	ρ_{rel} (%)	d ± s.d. (μm)
2.5	UA	1250	96.8	0.39 ± 0.19
5			96.9	0.26 ± 0.17
2.5		1300	99.0	0.48 ± 0.15
5			97.0	0.35 ± 0.20
2.5	PBM	1250	98.9	0.28 ± 0.14
5			97.3	0.23 ± 0.12
2.5		1300	100.0	0.31 ± 0.19
5			98.1	0.34 ± 0.19

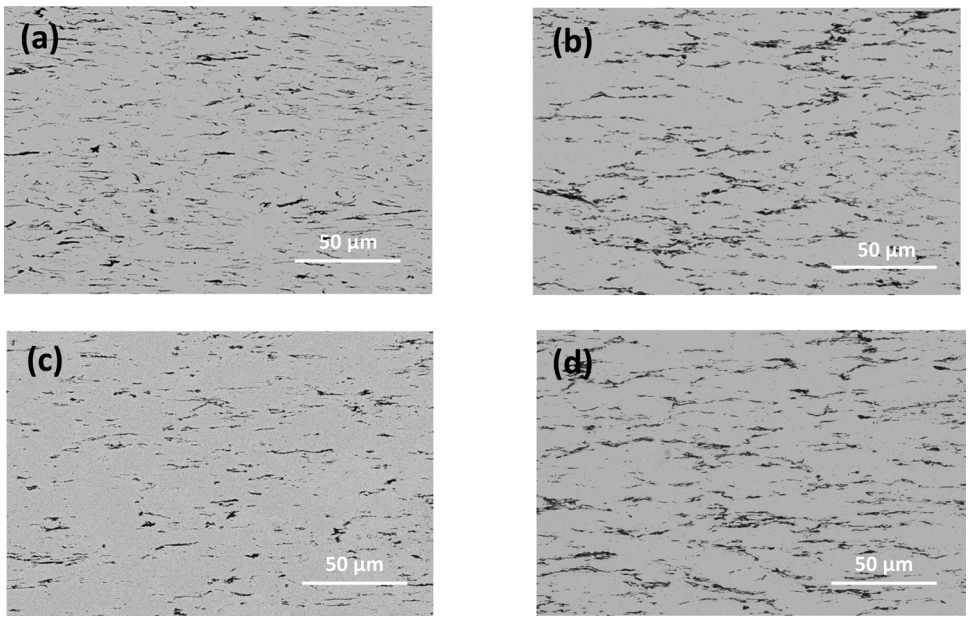

Fig. 5. BSE-SEM images from the cross section surfaces of the composites prepared by PBM with (a) and (c) 2.5 FLG vol%, and (b) and (d) 5 FLG vol%, and sintered at (a) and (b) 1250 °C, and (c) and (d) 1300 °C.

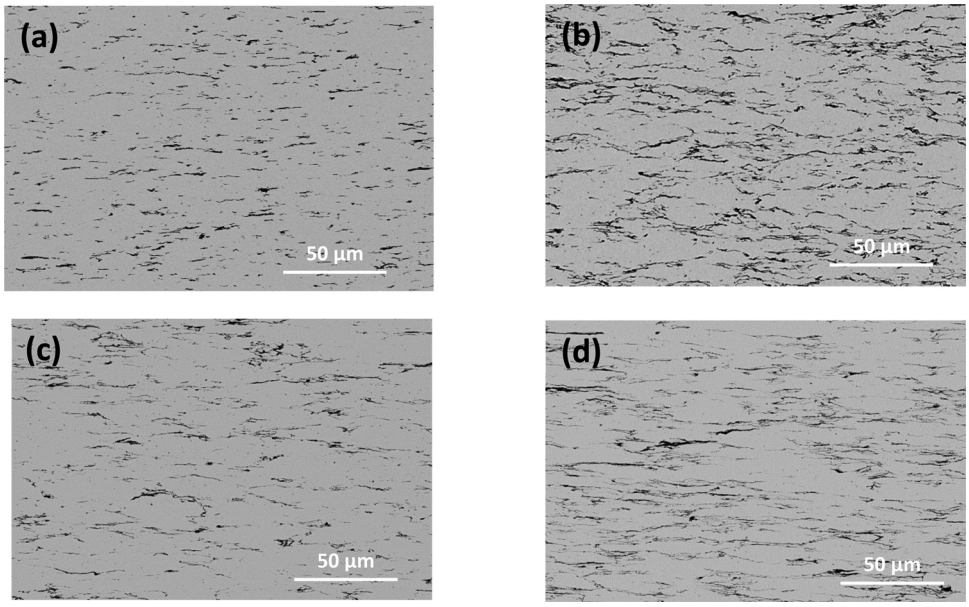

Fig. 6. BSE-SEM images from the cross section surfaces of the composites prepared by UA with (a) and (c) 2.5 FLG vol%, and (b) and (d) 5 FLG vol%, and sintered at (a) and (b) 1250 °C, and (c) and (d) 1300 °C.

Table 2
Electrical conductivity and anisotropy factor of the composites.

FLG vol%	Processing routine	Sintering T (°C)	$\sigma_{\perp}$ (S/m)	$\sigma_{//}$ (S/m)	$\sigma_{\perp}/\sigma_{//}$
2.5	UA	1250	Not conductive		—
5			421 ± 5	20.9 ± 0.7	20.1
2.5		1300	49.2 ± 0.9	3.06 ± 0.05	16.1
5			678 ± 11	73.9 ± 1.7	9.17
2.5	PBM	1250	Not conductive		—
5			173.8 ± 1.9	9.91 ± 0.09	17.5
2.5		1300	Not conductive		—
5			232 ± 8	13.42 ± 0.12	17.3

consequence of the improved crystallinity of FLG achieved by sintering at the highest temperature. An enhancement of electrical conductivity thanks to an optimization of the crystallinity has been also previously reported for alumina composites [21]. However, the increase in conductivity promoted by increasing the sintering temperature from 1250 to 1300 °C is not so noteworthy in the composites prepared by planetary ball milling. Moreover, lower conductivities were obtained in these composites, independently of the sintering temperature, when comparing with the ones prepared by ultrasonic agitation. Although the electrical conductivity might be also affected by the graphene nanoplatelets fragmentation during ball milling and their agglomeration, the lower conductivities in these composites can be also related to the higher amount of amorphous carbon present in the FLG in these composites, as shown in section §3.1.2. Thus, a connection between the

electrical conductivity in the composites and the presence of amorphous carbon in the FLG structure can be established.

Thanks to the adequate selection of processing and sintering conditions, the highest conductivity values achieved in this study are outstanding in comparison with the reported values for zirconia composites with GBN. The conductivity for the composite with 2.5 vol% FLG (~ 50 S/m) is much higher than the reported value for zirconia composites with 2.5 vol% rGO (~ 1.5 S/m) [20]. For the composite with 5 vol% FLG the conductivity reaches 680 S/m, a value much higher than the reported ones for zirconia composites with GNP (~ 45 S/m) [17] and rGO (~ 400 S/m) [20], and it is even higher than the reported value for zirconia composites with 10 vol% of exfoliated GNP (~ 470 S/m) [12].

4. Conclusions

In this work, the optimization of the few-layer graphene (FLG) crystallinity in highly dense zirconia composites prepared by two powder processing routines -ultrasonic agitation or planetary ball milling- and spark plasma sintered at two different temperatures has been analyzed in detail by Raman spectroscopy.

A significant enhancement of the FLG crystallinity, in terms of structural defects and amorphous carbon was achieved during the sintering process, being the improvement more remarkable when sintering at the highest temperature. However, a not negligible amount of amorphous carbon was remaining in the FLG structure in the composites prepared by planetary ball milling even after sintering at the highest temperature. As consequence, lower electrical conductivities were obtained in these composites in comparison with the ones prepared by ultrasonic agitation. The optimum results in terms of electrical conductivity were achieved for the composites prepared by ultrasonic agitation and sintered at 1300 °C, as a result of the enhanced FLG crystallinity achieved in these composites.

Declaration of Competing Interest

The authors declare that they have no known competing financial interests or personal relationships that could have appeared to influence the work reported in this paper.

Acknowledgements

This research was supported by the Ministerio de Ciencia, Innovación y Universidades (MCIU) under the project PGC 2018-101377-B-100 (MCIU/AEI/FEDER, UE). C. López-Pernía acknowledges the financial support of MINECO through the FPI contract ref: BES-2016-078711. C. Muñoz-Ferreiro acknowledges the financial support of a VI PPIT-US fellowship through the contract USE-18740-H. Dr. F. Gotor and Dr. J.M. Córdoba are also gratefully acknowledged for providing access to the planetary ball milling.

Appendix A. Supplementary data

Supplementary material related to this article can be found, in the online version, at doi:https://doi.org/10.1016/j.jeurceramsoc.2021.09.025.

References

[1] P. Miranzo, M. Belmonte, M.I. Osendi, From bulk to cellular structures: a review on ceramic/graphene filler composites, J. Eur. Ceram. Soc. 37 (2017) 3649–3672.
[2] A.G. Glukharev, V.G. Konakov, Synthesis and properties of zirconia-graphene composite ceramics: a brief review, Rev. Adv. Mater. Sci. 56 (2018) 124–138, https://doi.org/10.1515/rams-2018-0041.
[3] F. Li, L. Long, Y. Weng, A review on the contemporary development of composite materials comprising graphene/graphene derivatives, Adv. Mater. Sci. Eng. (2020) (2020) 1–16, https://doi.org/10.1155/2020/7915641.
[4] I. Ahmad, M. Islam, N.H. Alharthi, H. Alawadhi, T. Subhani, K.S. Munir, S.I. Shah, F. Inam, Y. Zhu, Chemical and structural analyses of the graphene nanosheet/alumina ceramic interfacial region in rapidly consolidated ceramic nanocomposites, J. Compos. Mater. 52 (2018) 417–428, https://doi.org/10.1177/0021998317708235.
[5] Z. Zeng, Y. Liu, W. Chen, X. Li, Q. Zheng, K. Li, R. Guo, Fabrication and properties of in situ reduced graphene oxide-toughened zirconia composite ceramics, J. Am. Ceram. Soc. 101 (2018) 3498–3507, https://doi.org/10.1111/jace.15483.
[6] C. Ramírez, Q. Wang, M. Belmonte, P. Miranzo, M. Isabel Osendi, B.W. Sheldon, N. P. Padture, Direct in situ observation of toughening mechanisms in nanocomposites of silicon nitride and reduced graphene-oxide, Scr. Mater. 149 (2018) 40–43, https://doi.org/10.1016/j.scriptamat.2018.02.004.
[7] S. Baskut, A. Cinar, A.T. Seyhan, S. Turan, Tailoring the properties of spark plasma sintered SiAlON containing graphene nanoplatelets by using different exfoliation and size reduction techniques: anisotropic electrical properties, J. Eur. Ceram. Soc. 38 (2018) 3787–3792, https://doi.org/10.1016/j.jeurceramsoc.2018.04.066.
[8] O. Hanzel, R. Sedlák, J. Sedláček, V. Bizovská, R. Bystrický, V. Girman, A. Kovalčíková, J. Dusza, P. Šajgalík, Anisotropy of functional properties of SiC composites with GNPs, GO and in-situ formed graphene, J. Eur. Ceram. Soc. 37 (2017) 3731–3739, https://doi.org/10.1016/j.jeurceramsoc.2017.03.060.
[9] C. Muñoz-Ferreiro, A. Morales-Rodríguez, T.C. Rojas, E. Jiménez-Piqué, C. López-Pernía, R. Poyato, A. Gallardo-López, Microstructure, interfaces and properties of 3YTZP ceramic composites with 10 and 20 vol% different graphene-based nanostructures as fillers, J. Alloys. Compd. 777 (2019) 213–224, https://doi.org/10.1016/j.jallcom.2018.10.336.
[10] O. Hanzel, M.A. Singh, D. Marla, R. Sedlák, P. Šajgalík, Wire electrical discharge machinable SiC with GNPs and GO as the electrically conducting filler, J. Eur. Ceram. Soc. 39 (2019) 2626–2633, https://doi.org/10.1016/j.jeurceramsoc.2019.03.012.
[11] F. Zeller, C. Müller, P. Miranzo, M. Belmonte, Exceptional micromachining performance of silicon carbide ceramics by adding graphene nanoplatelets, J. Eur. Ceram. Soc. 37 (2017) 3813–3821, https://doi.org/10.1016/j.jeurceramsoc.2017.03.072.
[12] C. López-Pernía, C. Muñoz-Ferreiro, C. González-Orellana, A. Morales-Rodríguez, Á. Gallardo-López, R. Poyato, Optimizing the homogenization technique for graphene nanoplatelet/yttria tetragonal zirconia composites: influence on the microstructure and the electrical conductivity, J. Alloys. Compd. 767 (2018) 994–1002, https://doi.org/10.1016/j.jallcom.2018.07.199.
[13] Á. Gallardo-López, J. Castillo-Seoane, C. Muñoz-Ferreiro, C. López-Pernía, A. Morales-Rodríguez, R. Poyato, Flexure strength and fracture propagation in zirconia ceramic composites with exfoliated graphene nanoplatelets, Ceramics 3 (2020) 78–91.
[14] O. Tapasztó, V. Puchy, Z.E. Horváth, Z. Fogarassy, E. Bódis, Z. Károly, K. Balázsi, J. Dusza, L. Tapasztó, The effect of graphene nanoplatelet thickness on the fracture toughness of Si3N4 composites, Ceram. Int. 45 (2019) 6858–6862, https://doi.org/10.1016/j.ceramint.2018.12.180.
[15] H. Xia, X. Zhang, Z. Shi, C. Zhao, Y. Li, J. Wang, G. Qiao, Mechanical and thermal properties of reduced graphene oxide reinforced aluminum nitride ceramic composites, Mater. Sci. Eng. A 639 (2015) 29–36, https://doi.org/10.1016/j.msea.2015.04.091.
[16] C. Ramirez, P. Miranzo, M. Belmonte, M.I. Osendi, P. Poza, S.M. Vega-Diaz, M. Terrones, Extraordinary toughening enhancement and flexural strength in Si3N4 composites using graphene sheets, J. Eur. Ceram. Soc. 34 (2014) 161–169, https://doi.org/10.1016/j.jeurceramsoc.2013.08.039.
[17] R. Poyato, J. Osuna, A. Morales-Rodríguez, Á. Gallardo-López, Electrical conduction mechanisms in graphene nanoplatelet/yttria tetragonal zirconia composites, Ceram. Int. 44 (2018) 14610–14616, https://doi.org/10.1016/j.ceramint.2018.05.082.
[18] X.Y. Fang, X.X. Yu, H.M. Zheng, H.B. Jin, L. Wang, M.S. Cao, Temperature- and thickness-dependent electrical conductivity of few-layer graphene and graphene nanosheets, Phys. Lett. Sect. A Gen. At. Solid State Phys. 379 (2015) 2245–2251, https://doi.org/10.1016/j.physleta.2015.06.063.
[19] J.-H. Shin, J. Choi, M. Kim, S.-H. Hong, Comparative study on carbon nanotube- and reduced graphene oxide-reinforced alumina ceramic composites, Ceram. Int. 44 (2018) 8350–8357, https://doi.org/10.1016/j.ceramint.2018.02.024.
[20] C. López-Pernía, A. Morales-Rodríguez, Á. Gallardo-López, R. Poyato, Enhancing the electrical conductivity of in-situ reduced graphene oxide-zirconia composites through the control of the processing routine, Ceram. Int. 47 (2021) 9382–9391, https://doi.org/10.1016/j.ceramint.2020.12.069.
[21] F. Inam, T. Vo, B.R. Bhat, Structural stability studies of graphene in sintered ceramic nanocomposites, Ceram. Int. 40 (2014) 16227–16233, https://doi.org/10.1016/j.ceramint.2014.07.058.
[22] X. Wang, J. Zhao, E. Cui, H. Liu, Y. Dong, Z. Sun, Effects of sintering parameters on microstructure, graphene structure stability and mechanical properties of graphene reinforced Al2O3-based composite ceramic tool material, Ceram. Int. 45 (2019) 23384–23392, https://doi.org/10.1016/j.ceramint.2019.08.040.
[23] M.A. Pimenta, G. Dresselhaus, M.S. Dresselhaus, L.G. Cançado, A. Jorio, R. Saito, Studying disorder in graphite-based systems by Raman spectroscopy, Phys. Chem. Chem. Phys. 9 (2007) 1276–1291, https://doi.org/10.1039/b613962k.
[24] L.M. Malard, M.A. Pimenta, G. Dresselhaus, M.S. Dresselhaus, Raman spectroscopy in graphene, Phys. Rep. 473 (2009) 51–87, https://doi.org/10.1016/j.physrep.2009.02.003.
[25] E.H. Martins Ferreira, M.V.O. Moutinho, F. Stavale, M.M. Lucchese, R.B. Capaz, C. A. Achete, A. Jorio, Evolution of the Raman spectra from single-, few-, and many-layer graphene with increasing disorder, Phys. Rev. B - Condens. Matter Mater. Phys. 82 (2010), 125429, https://doi.org/10.1103/PhysRevB.82.125429.

[26] A. Eckmann, A. Felten, A. Mishchenko, L. Britnell, R. Krupke, K.S. Novoselov, C. Casiraghi, Probing the nature of defects in graphene by Raman spectroscopy, Nano Lett. 12 (2012) 3925–3930, https://doi.org/10.1021/nl300901a.
[27] A.C. Ferrari, D.M. Basko, Raman spectroscopy as a versatile tool for studying the properties of graphene, Nat. Nanotechnol. 8 (2013) 235–246, https://doi.org/10.1038/nnano.2013.46.
[28] X. Díez-Betriu, S. Álvarez-García, C. Botas, P. Álvarez, J. Sánchez-Marcos, C. Prieto, R. Menéndez, A. De Andrés, Raman spectroscopy for the study of reduction mechanisms and optimization of conductivity in graphene oxide thin films, J. Mater. Chem. C 1 (2013) 6905–6912, https://doi.org/10.1039/c3tc31124d.
[29] P. Venezuela, M. Lazzeri, F. Mauri, Theory of double-resonant Raman spectra in graphene: intensity and line shape of defect-induced and two-phonon bands, Phys. Rev. B - Condens. Matter Mater. Phys. 84 (2011) 1–25, https://doi.org/10.1103/PhysRevB.84.035433.
[30] A. Gallardo-López, I. Márquez-Abril, A. Morales-Rodríguez, A. Muñoz, R. Poyato, Dense graphene nanoplatelet/yttria tetragonal zirconia composites: processing, hardness and electrical conductivity, Ceram. Int. 43 (2017) 11743–11752, https://doi.org/10.1016/j.ceramint.2017.06.007.
[31] C. Ramirez, M.I. Osendi, Characterization of graphene nanoplatelets-Si3N4 composites by Raman spectroscopy, J. Eur. Ceram. Soc. 33 (2013) 471–477, https://doi.org/10.1016/j.jeurceramsoc.2012.09.014.
[32] A.C. Ferrari, J.C. Meyer, V. Scardaci, C. Casiraghi, M. Lazzeri, F. Mauri, S. Piscanec, D. Jiang, K.S. Novoselov, S. Roth, A.K. Geim, Raman spectrum of graphene and graphene layers, Phys. Rev. Lett. 97 (2006) 1–4, https://doi.org/10.1103/PhysRevLett.97.187401.
[33] F. Herziger, C. Tyborski, O. Ochedowski, M. Schleberger, J. Maultzsch, Double-resonant la phonon scattering in defective graphene and carbon nanotubes, Phys. Rev. B - Condens. Matter Mater. Phys. 90 (2014), https://doi.org/10.1103/PhysRevB.90.245431.
[34] D. López-Díaz, M. López Holgado, J.L. García-Fierro, M.M. Velázquez, Evolution of the Raman spectrum with the chemical composition of graphene oxide, J. Phys. Chem. C 121 (2017) 20489–20497, https://doi.org/10.1021/acs.jpcc.7b06236.
[35] S. Claramunt, A. Varea, D. López-Díaz, M.M. Velázquez, A. Cornet, A. Cirera, The importance of interbands on the interpretation of the Raman spectrum of graphene oxide, J. Phys. Chem. C 119 (2015) 10123–10129, https://doi.org/10.1021/acs.jpcc.5b01590.
[36] S. Vollebregt, R. Ishihara, F.D. Tichelaar, Y. Hou, C.I.M. Beenakker, Influence of the growth temperature on the first and second-order Raman band ratios and widths of carbon nanotubes and fibers, Carbon N.Y. 50 (2012) 3542–3554, https://doi.org/10.1016/j.carbon.2012.03.026.
[37] A. Sadezky, H. Muckenhuber, H. Grothe, R. Niessner, U. Pöschl, Raman microspectroscopy of soot and related carbonaceous materials: spectral analysis and structural information, Carbon N.Y. 43 (2005) 1731–1742, https://doi.org/10.1016/j.carbon.2005.02.018.
[38] A.C. Ferrari, J. Robertson, Interpretation of Raman spectra of disordered and amorphous carbon, Phys. Rev. B 61 (2000) 14 095–14 107.
[39] R. Poyato, R. Verdugo, C. Muñoz-Ferreiro, Á. Gallardo-López, Electrochemically exfoliated graphene-like nanosheets for use in ceramic nanocomposites, Materials (Basel) 13 (2020) 2656, https://doi.org/10.3390/ma13112656.
[40] T. Jawhari, A. Roid, J. Casado, Raman spectroscopic characterization of some commercially available carbon black materials, Carbon N.Y. 33 (1995) 1561–1565, https://doi.org/10.1016/0008-6223(95)00117-V.
[41] Y. Dong, S. Zhang, X. Du, S. Hong, S. Zhao, Y. Chen, X. Chen, H. Song, Boosting the electrical double-layer capacitance of graphene by self-doped defects through ball-milling, Adv. Funct. Mater. 29 (2019) 1–10, https://doi.org/10.1002/adfm.201901127.
[42] Y. Dong, X. Lin, D. Wang, R. Yuan, S. Zhang, X. Chen, L.G. Bulusheva, A. V. Okotrub, H. Song, Modulating the defects of graphene blocks by ball-milling for ultrahigh gravimetric and volumetric performance and fast sodium storage, Energy Storage Mater. 30 (2020) 287–295, https://doi.org/10.1016/j.ensm.2020.05.016.
[43] C. Androulidakis, E.N. Koukaras, J. Parthenios, G. Kalosakas, K. Papagelis, C. Galiotis, Graphene flakes under controlled biaxial deformation, Sci. Rep. 5 (2015) 1–11, https://doi.org/10.1038/srep18219.